ORIGINAL PAPER

Composite cathode materials Ag-Ba$_{0.5}$Sr$_{0.5}$Co$_{0.8}$Fe$_{0.2}$O$_3$ for solid oxide fuel cells

Michał Mosiałek · Magdalena Dudek · Aneta Michna · Maciej Tatko · Aneta Kędra · Małgorzata Zimowska

Abstract Silver-Ba$_{0.5}$Sr$_{0.5}$Co$_{0.8}$Fe$_{0.2}$O$_{3-\delta}$ (BSCF) cathodes were prepared in two ways. In the first method, Ag-BSCF composite powder was prepared in ethanol solution, where Ag nanoparticles serving as a component in the preparation of Ag-BSCF composite cathodes had been previously obtained via one-step synthesis in absolute ethanol using a neutral polymer (polyvinylpyrrolidone). To the best of our knowledge, this is the first study to use a Ag sol obtained by the above method for preparation of Ag-BSCF composite powder. Then, a paste containing this powder was screen-printed on a Sm$_{0.2}$Ce$_{0.8}$O$_{1.9}$ electrolyte and sintered at 1,000 °C. In the second technique, an aqueous solution of AgNO$_3$ was added to a previously sintered BSCF cathode, which was then sintered again at 800 °C. The oxygen reduction reaction at the quasi-point BSCF cathode on the Sm$_{0.2}$Ce$_{0.8}$O$_{1.9}$ electrolyte was tested by electrochemical impedance spectroscopy at different oxygen concentrations in three electrode setup. The continuous decrease of polarization resistance was observed under polarization −0.5 V at 600 °C. The comparative studies of both obtained composite Ag-BSCF materials were performed in hydrogen-oxygen IT-SOFC involving samaria-doped ceria as an electrolyte and Ni-Gd$_{0.2}$Ce$_{0.8}$O$_{1.9}$ anode. In both cases, the addition of silver to the cathode caused an increase in current and power density compared with an IT-SOFC built with the same components but involving a monophase BSFC cathode material.

Introduction

Nowadays, efforts in the domain of solid oxide fuel cells (SOFCs) are focused on devices capable of operating within an intermediate temperature (IT) range (500–700 °C). In this range, the main polarization losses occur on the cathode. La$_{0.8}$Sr$_{0.2}$MnO$_{3-\delta}$ (LSM), a commonly used cathode material within higher temperature ranges, exhibits high polarization resistance below 800 °C [1, 2]. Other manganites also exhibit polarization resistances two orders greater than cobaltites in the IT range [2]. Among other new materials, Ba$_{0.5}$Sr$_{0.5}$Co$_{0.8}$Fe$_{0.2}$O$_{3-\delta}$ (BSCF) perovskite seems to be a promising candidate. BSCF, first described by Shao and Haile [3], was the subject of numerous papers reviewed in 2009 by Zhu et al. [4].

Shao and Haile [3] reported values of peak power density for cells with BSCF cathodes more than twice those measured for a similar cell that used Sc$_{0.5}$Sm$_{0.5}$CoO$_{3-\delta}$ (SSC)+ Sm$_{0.2}$Ce$_{0.8}$O$_{1.9}$ (samaria-doped ceria (SDC)) as a cathode. Baumann et al. [5, 6] compared BSCF, La$_{0.6}$Sr$_{0.4}$CoO$_{3-\delta}$ (LSC), La$_{0.6}$Sr$_{0.4}$Co$_{0.8}$Fe$_{0.2}$O$_{3-\delta}$ LSCF, La$_{0.6}$Sr$_{0.4}$FeO$_{3-\delta}$ (LSF), and SSC cathodes. The authors showed that among these cobaltites and ferrites, BSCF has the lowest surface exchange resistance; for example, electrochemical surface exchange at a BSCF microelectrode was 50 times lower than at a similar LSCF microelectrode. Liu et al. [7] compared anode-supported SOFCs based on a Gd$_{0.2}$Ce$_{0.8}$O$_{1.9}$ (gadolinia-doped ceria (GDC)) electrolyte 10-μm thick. The authors concluded that a BSCF cathode shows a much lower interfacial polarization resistance at low temperatures (450–600 °C) than LSCF- and SSC-based cathodes. Kim et al. [8]

M. Mosiałek (✉) · A. Michna · M. Tatko · A. Kędra · M. Zimowska
Jerzy Haber Institute of Catalysis and Surface Chemistry PAS, Niezapominajek 8, 30-239 Cracow, Poland
e-mail: nbmosial@cyfronet.pl

M. Dudek
Faculty of Fuels and Energy, AGH—University of Science and Technology, Cracow, Poland

compared metal-supported cells with unsintered BSCF, LSCF, and LSM cathode materials. They found that the lowest polarization resistance is exhibited by BSCF cathodes, and obtained the greatest peak power density for cells with BSCF cathode material. BSCF reveals some degree of instability. It reacts with CO_2 present in oxidant gaseous mixtures, forming oxides and carbonates [9] as follows:

$$Ba_{0.5}Sr_{0.5}Co_{0.8}Fe_{0.2}O_3 + CO_2 \rightarrow Ba_{0.5}Sr_{0.5}CO_3 + 0.8CoO \quad (1)$$
$$+ 0.4\ O_2 + 0.1Fe_2O_3$$
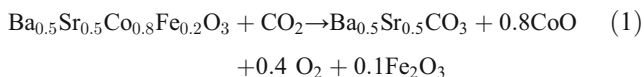
The reverse reaction occurs at temperatures higher than 807 °C and is also used in the synthesis of BSCF [10, 11]. Yan et al. [12] examined the adsorption and desorption of CO_2 on a BSCF surface and concluded that CO_2 can adsorb and react with BSCF from 400 to 700 °C to form $Sr_{0.6}Ba_{0.4}CO_3$. The other disadvantage of BSCF is low electronic conductivity: 40–60 S cm^{-1} [13, 14]. The addition of second phase with high electric conductivity should lead to improved cathode performance [14]. Zhou et al. [14] used $LaCoO_3$ (LC), which revealed that electric conductivity of 1,000 S cm^{-1} was achieved by a BSCF-LC composite cathode with an electric conductivity of 300 S cm^{-1}, although the authors observed a rise in both polarization resistance R_p and ohmic resistance of the cell R_{ohm}, along with rising LC content.

Silver has the greatest electric conductivity among metals. Silver exhibits excellent electrocatalytic properties in oxygen reduction reaction (ORR) and the lowest cathodic overpotential resistance (among Ag, Au, Pt, LSC, LSM, LSCF, and $La_{0.6}Sr_{0.4}Fe_{0.8}Mn_{0.2}O_3$) [15]. Pure silver is not used as a cathode in SOFC due to its disadvantages.

Silver moves rapidly under negative polarization, changing electrode geometry [16], which causes a rise in electrode performance at an early stage but can lead to the separation of silver from a composite cathode at the electrode/electrolyte interface [17]. Silver electrodes reveal high polarization resistances reported on both quasi-point [18] and porous electrodes [19]. Composite cathodes with silver and ionic conductor material are characterized by good performance [17, 20–27]. Many composites containing silver and oxide cathode material, such as LSCF, LSM, SSC, $La_{1.6}Sr_{0.4}NiO_4$, and BSCF, exhibit better electrochemical performance than the same materials without silver [13, 16, 28–39]. Moreover, silver is used in current collectors and as a sealant [40, 41]. The abovementioned composites reveal considerable stability. Sasaki et al. [27] found no structural changes in an Ag-SSC composite electrode following −0.5 V polarization. Simner et al. [42] reported that cells with Ag-LSCF and Ag-SSC composite cathodes worked for nearly 2,000 h at 650 °C with stable power output. Sarikaya et al. [43] reported that porous Ag-LSM composite current collector worked for 5,000 h at 800 °C with stable electrical properties and no microstructural degradation.

Silver current collectors are used frequently. Shao and Haile [3] supposed that silver in current collectors does not affect cathode performance. A conflicting assumption was drawn from data presented by Gou et al. [19, 41]. Similar cells differing only in terms of current collectors (Au, Ag) with BSCF or SSC cathodes were compared [19]. The use of silver as the current collector for a BSCF electrode was accompanied by lower area-specific resistance (ASR) and improved cell performance compared to a cell with a gold current collector [19]. Silver is a good catalyst for oxygen surface adsorption, dissociation of molecular oxygen into atomic oxygen, and oxygen surface diffusion, improving the overall oxygen surface exchange kinetics of BSCF electrodes [19]. Five different current collection techniques using Ag and LC were compared [41]. BSCF cathodes with a current collector made of diluted silver paste exhibited an ASR seven times lower than that of a similar cathode without a current collector, whereas the peak power density of cells containing these cathodes measured at 600 °C were 960 and 30 mW cm^{-2}, respectively.

Zhang et al. [44] prepared a composite Ag-BSCF cathode using a paste containing 14 % silver. These authors reported that the introduction of either SDC or Ag into the BSCF cathode lowered the performance of the cells. Su et al. [35, 37] prepared the Ag-BSCF composite using a vacuum-assisted electroless Ag deposition. The fabrication of a silver-modified BSCF cathode was performed in a vacuum (<20 kPa) by using aqueous solutions of $AgNO_3$ and formaldehyde as a reducing agent. The authors demonstrated that the presence of Ag significantly reduced the electrode's ohmic resistance and enhanced the catalytic O_2 reduction performance of the BSCF cathode. Zhou at al. [38] compared Ag-BSCF composite cathodes obtained using hydrazine or formaldehyde and concluded that the application of formaldehyde could lead to the formation of the carbonate $Ba_xSr_{1-x}CO_3$, which poisons active sites for oxygen adsorption and inhibits ORR.

However, silver has a low melting temperature (961 °C), whereas most perovskite-based cathodes should be sintered at 1,000–1,100 °C. For this reason, composite cathodes were prepared in a two-step sintering procedure. First, the BSCF cathode was fired at a high optimized temperature, then soaked in a solution containing silver nitrate and reducing agent and fired again at a lower temperature [35–38].

Several one-step sintering procedures for silver perovskite cathodes have been proposed as follows: (i) Simner et al. [29] used a mechanofusion dry processing method to prepare the Ag-LSCF composite cathode; (ii) silver-perovskite composite powder was obtained by adding silver nitrate to the starting nitrate solution during the synthesis of perovskite [33, 45, 46]; (iii) silver paste was screen-printed prior to the perovskite paste, forming a layer of silver between the perovskite and electrolyte [47].

As has been pointed out, recent developments have intensified the need for the preparation of composite cathodes

containing perovskite and silver. In our opinion, efforts should be focused on the preparation of well-dispersed silver nanoparticles and their incorporation into the skeleton of oxide cathode material such as BSCF. To synthesize the silver nanoparticles, a physical [48], biochemical [49], or chemical method (e.g., synthesis in aqueous solution [50]) can be applied. Furthermore, an alternative method for the preparation of silver sol might be the reduction of silver nitrate with absolute ethanol in the presence of a polymer [51]. As was proved in [51], silver nanoparticles characterized by fine dispersion and narrow-size distribution can be obtained by this technique.

Comparison of the electrochemical performance of various cathode materials has usually been performed by measuring the power output of fuel cells or by electrochemical measurements (electrochemical impedance spectroscopy (EIS), cyclic voltammetry (CV), and long-time polarization) of cathode properties in argon-oxygen mixtures. These measurements have been performed using point electrodes [5, 6, 15, 18, 52–54], porous electrodes in a symmetrical cell [55–59], or three-electrode setup [60–62].

In the present study, a new wet route for synthesis of evenly dispersed Ag-BSCF composite material for the preparation of cathodes in one sintering step is proposed. Ag nanoparticles were obtained via one-step synthesis by using absolute ethanol and a neutral polymer (polyvinylpyrrolidone). Then, BSCF powder was added to the obtained silver sol and metal nanoparticles were incorporated into the BSCF oxide powder. Next, the cathode was sintered in a one-step process. To the best of our knowledge, this is the first study which uses the Ag sol obtained using the above method for preparation of the Ag-BSCF composite. The performance of a cell with the new Ag-BSCF composite cathode is compared with that of a similar cell containing a Ag-BSCF composite cathode obtained using a different method.

Experimental

Materials

Synthesis of BSCF

BSCF was prepared from a nitrate solution using the Pechini method. The starting materials were $Ba(NO_3)_2$ (99.5 %, POCH), $Sr(NO_3)_2$ (99 %, POCH), $Fe(NO_3)_3$ $9H_2O$ (99 %, POCH), $Co(NO_3)_2$ $6H_2O$ (99 %, POCH), citric acid (99.5 %, POCH), and ethylene glycol (99.9 %, POCH). The reagents were mixed in distilled water in stoichiometric proportions to prepare a compound of the composition $Ba_{0.6}Sr_{0.4}Co_{0.8}Fe_{0.2}O_3$. Citric acid and ethylene glycol were added to the respective nitrate solutions. The solutions were then evaporated at 180 °C for 12 h, then at 200 °C for the next 12 h, and finally at 220 °C to remove gaseous reactants. The obtained material was calcined at 1,100 °C for 3 h and then rotary-vibratory milled with zirconia grinding media in dry ethanol (Fig. 1).

Synthesis of samaria-doped ceria

$Ce_{0.8}Sm_{0.2}O_{1.9}$ powder was prepared using $Ce(NO_3)_3$ $6H_2O$ and $Sm(NO_3)_3$ $6H_2O$ (both 99.99 % purity, supplied by Aldrich). Aqueous NH_3 solution was used as a precipitating agent. The aqueous solution, containing both cations in proper ratio, was slowly added to the continuously-stirred 25 % NH_3 solution; finally, the pH was adjusted to 10 with the NH_3 solution. The precipitate was washed with distilled water, calcined at 800 °C for 1 h, and ground in ethyl alcohol in a rotary-vibratory mill with zirconia grinding media. The samples were formed into disks 19.8 mm in diameter and 1.8–2.0 mm thick, and sintered at 1,500 °C for 2 h. The relative density of such prepared samples was at least 98 %. The X-ray

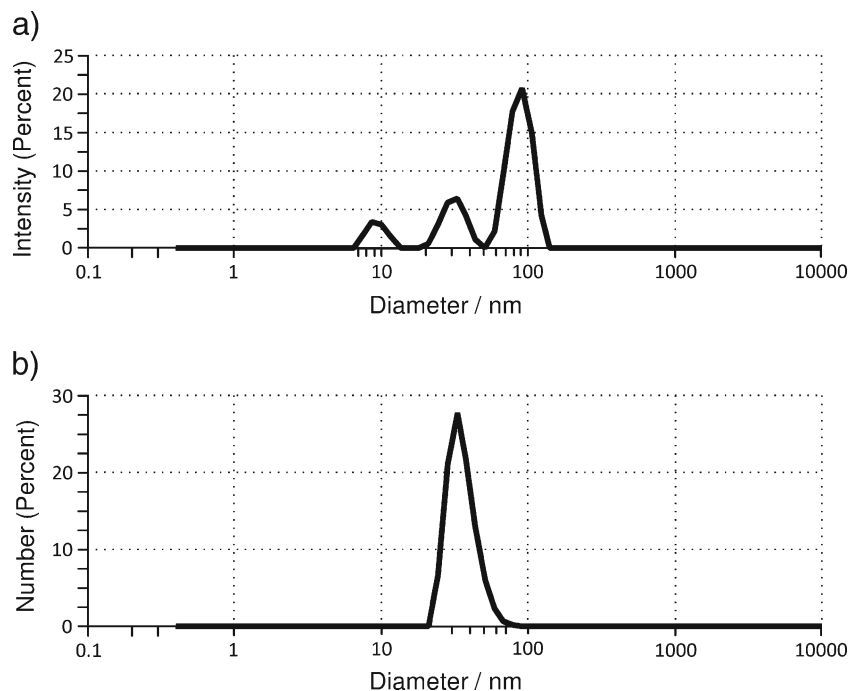Fig. 1 The diffraction pattern of obtained BSCF powder
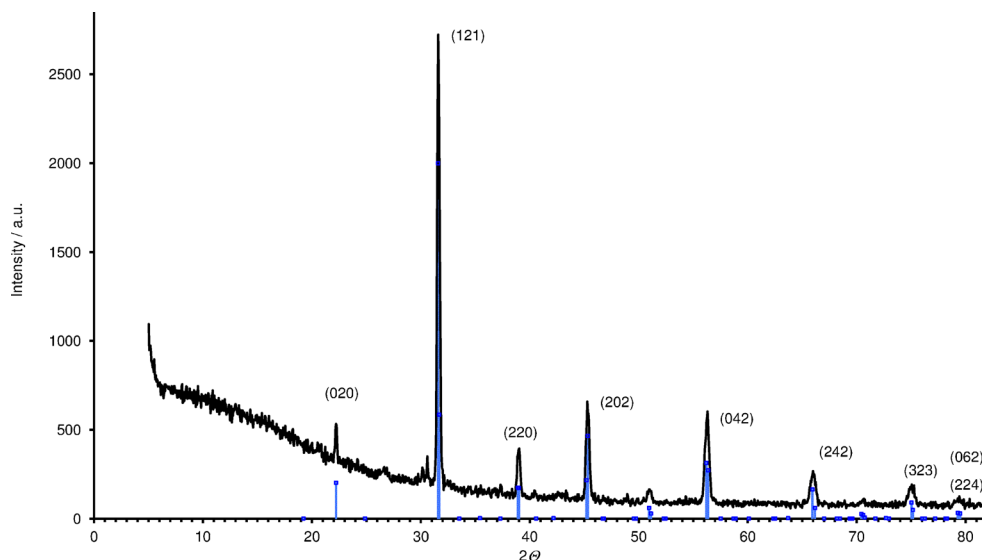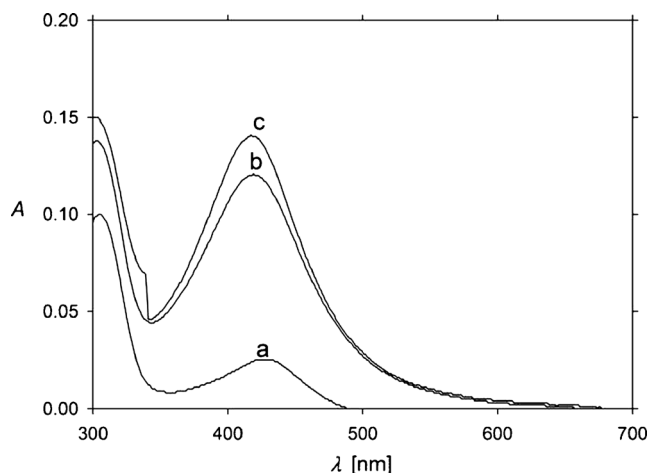
Fig. 2 The UV–Vis adsorption spectra obtained from silver sol at various times of synthesis: **a** 100 min, **b** 200 min, and **c** 280 min. The peak of the maximum absorption occurs at λ_{max}=418 nm

diffraction (XRD) analysis method determined that only cubic samaria-ceria solid solution had been obtained. The physico-chemical properties of sintered SDC samples as electrolytic material were described in the previous paper [63].

Synthesis of silver nanoparticles and preparation of Ag-BSCF composite powders

The precursor used to synthesize colloidal silver was silver nitrate (Chempur). Polyvinylpyrrolidone (PVP; M_w= 29,000 Da) and ethanol (pure 99.8 %) were purchased from Sigma-Aldrich and Avantor Performance Materials Poland S.A., respectively.

In order to determine the average size of synthesized silver nanoparticles, they were deposited on natural ruby mica sheets (Continental Trade, Poland).
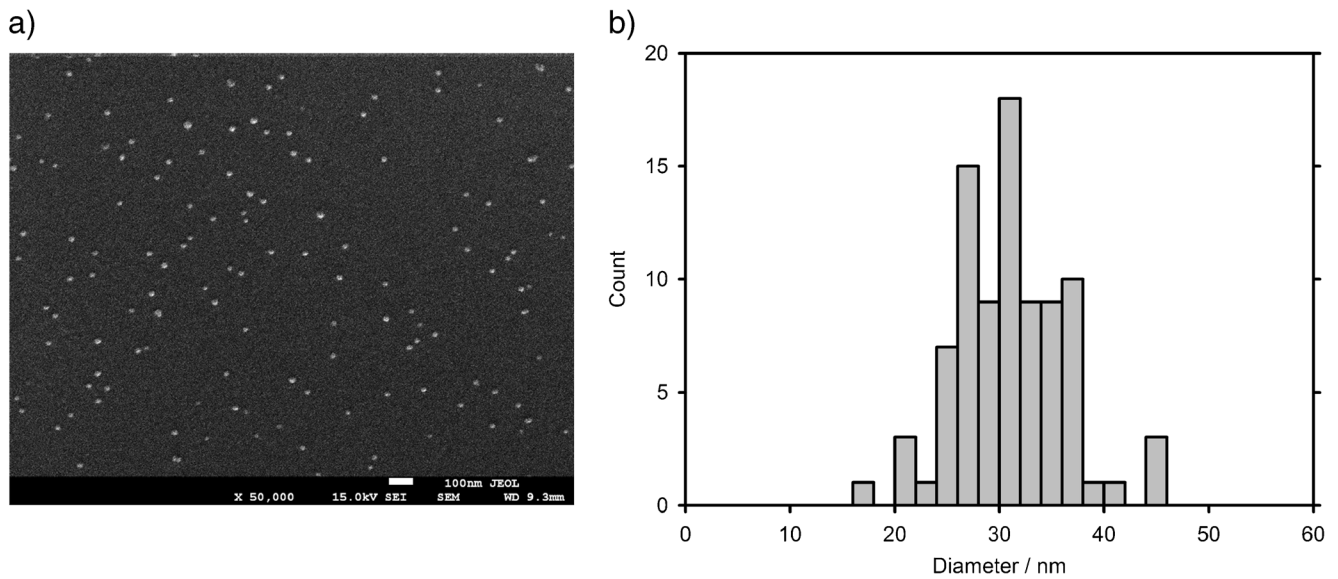
Prior to the experiments, all glassware was cleaned with a strong surfactant (Mucasol), and ultrapure water (Elix and Simplicity 185 system; Millipore SAS, Molsheim, France).

Silver sol was prepared according to the modified method described by Kim [64] through the reduction of silver nitrate by ethanol in the presence of PVP, serving as a protective agent.

In a typical synthesis, 0.237 g of $AgNO_3$, 100 ml ethyl alcohol, and PVP were added into a 250-ml round-bottomed flask equipped with a magnetic stirring bar and thermocontroller. The flask was placed in a water bath and all components were vigorously mixed with the magnetic stirrer at 50 °C for 5 h. Over time, the solution gradually turned yellow, and the evolution of stable dispersion of silver nanoparticles was observed.

During the synthesis, samples of silver sol were removed from the reaction mixture at various time intervals (100, 200, and 280 min) and placed in quartz cuvettes. Then, the UV–Vis adsorption spectra of samples were measured by a Shimadzu UV-1800 spectrophotometer.

In Fig. 2, the UV–Vis absorption spectra of silver sol sampled at various points during synthesis are presented. As can be observed, a broad peak appeared at the reaction time of 100 min, suggesting the formation of the first silver nanoparticles. However, the intensity of the adsorption peak around 418 nm, attributed to the surface plasmon band of Ag nanoparticles, did not increase strongly until approximately 200 min of synthesis. Furthermore, this peak (marked as b) was sharper than the previous one (marked as a). This

Fig. 3 Size distribution of silver nanoparticles **a** by intensity, and **b** by number determined by DLS method

a)

b)

Fig. 4 **a** The SEM image of silver particles on mica (scan bar=100 nm); **b** histogram of the size distribution of the particles. The average diameter of particles is equal to 31 nm

observation can be explained by the increased concentration of silver nanoparticles in the sol. Additionally, the intensity of the surface plasmon band changed insignificantly, from 200 to 280 min, suggesting that the reduction process of silver nitrate was almost complete.

In order to determine the exact size of the silver nanoparticles, two complementary methods, dynamic light scattering (DLS) and scanning electron microscopy (SEM), were applied.

In the DLS technique, the size (hydrodynamic diameter) d_H of silver nanoparticles was calculated using the Stokes-Einstein equation as follows:

$$d_H = \frac{kT}{3\pi\eta D} \qquad (2)$$

where D is the diffusion coefficient of particles measured in bulk by a Malvern Zetasizer Nano ZS instrument, k is the Boltzmann constant, and T is the absolute temperature.

The size distributions of synthesized silver particles by intensity and by number are presented in Fig. 3a, b, respectively. As can be seen, three peaks with maxima assuming the values 9, 36, and 92 nm were obtained (see Fig. 3a). However, in Fig. 3b, only one peak with a maximum at 36 nm was observed. Thus, it can be concluded that 36-nm particles occurred in the largest numbers in the synthesized silver suspension.

To confirm this hypothesis, the average size of particles was measured using the SEM technique, in which a drop of silver suspension was first placed on the surface of a freshly cloven mica sheet. Then, silver nanoparticles deposited on mica were air-dried and analyzed using the SEM technique. A typical micrograph can be seen in Fig. 4a. Size (diameter) was calculated as the averaged value of measurements in two perpendicular directions. According to the histogram presented in Fig. 4b, the average

Fig. 5 Schematic views: **a** alumina test fixture, **b** cross-section of the inner tube, **c, d** electrochemical cell with investigated quasi-point, BSCF reference, and LSCF counter electrodes; *1* outer alumina tube, *2* inner alumina tube, *3* spring, *4* central canal, *5* canal, *6* platinum wire, *7* alumina rod, *8* thermocouple, *9* canal with platinum wire, *10* electrochemical cell, *11* alumina distance, *12* electrolyte, *13* electrodes, *14* LSCF counter electrode, *15* SUS 430 steel interconnector, *16* platinum foil current collector, *17* BSCF quasi-point (bar) electrode
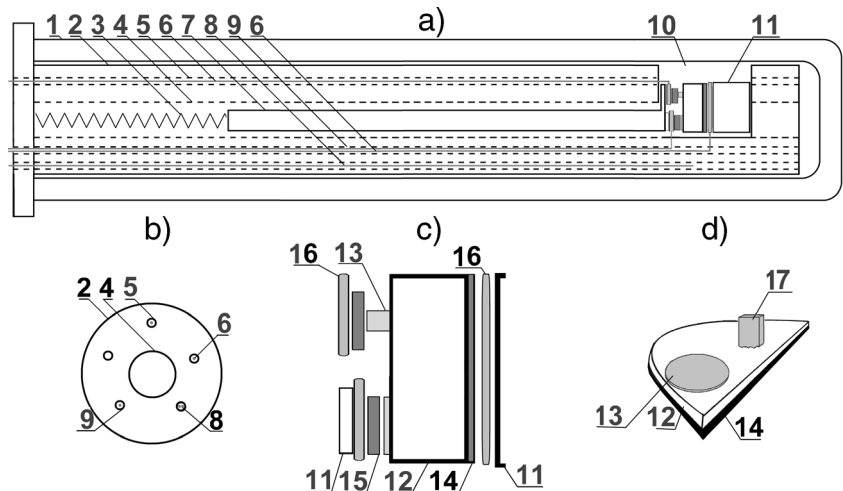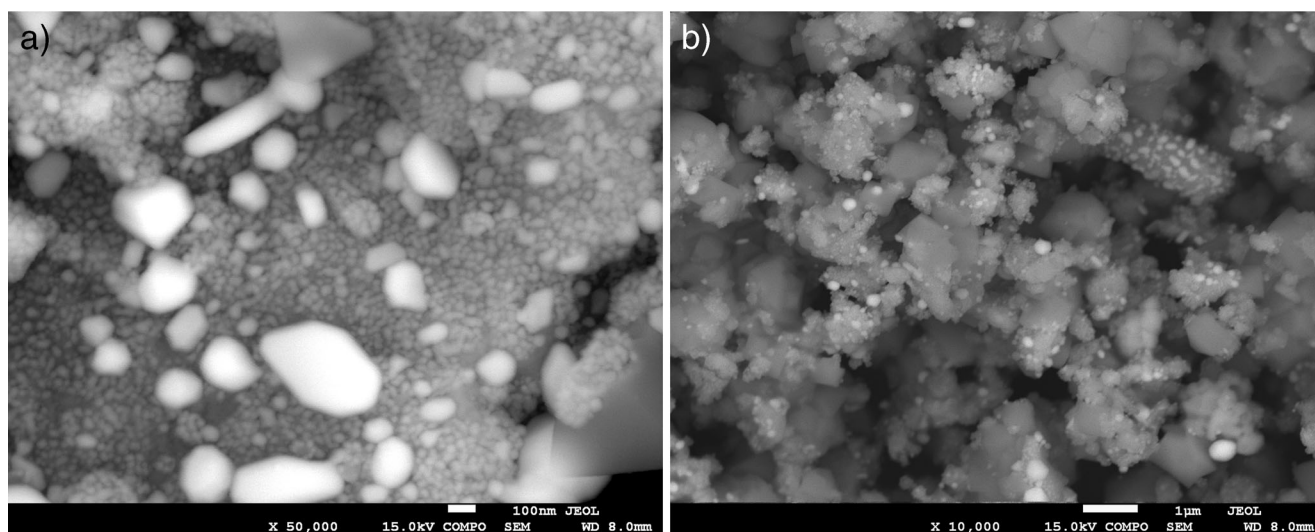
Fig. 6 Images of Ag-BSCF composite powders determined by the SEM method in COMPO mode

diameter of nanoparticles was 31 nm, which correlated well with the average size (by number) equal to 36 nm obtained by DLS.

In the second step, Ag-BSCF composite powder was prepared. The obtained silver sol was added to a stirred ultrafiltration cell (Millipore, Model 8400) followed by the addition of 0.2882 g of BSCF powder (ground for 20 h at 250 rpm). Vigorous stirring was maintained throughout the entire process of Ag-BSCF composite formation, i.e., 60 min. To separate the Ag-BSCF powder from ethanol, the mixture was left in the ultrafiltration cell for 60 min and then the ethanol was gently decanted. The obtained precipitate was dried under argon at 25 °C.

*Preparation of porous electrodes for EIS measurements*

The LSCF porous counter electrode was fabricated by screen-printing LSCF paste (Fuel Cells Materials Inc.) on the entire rear side of the electrolyte disk (20-mm diameter), which was then dried and fired at 1,100 °C for 2 h with a heating and cooling rate of 1 °C min^{-1}. The disk was cut in half and the reference electrode was made on the front side of the disk (see Fig. 5d) as described below.

BSCF powder and an organic vehicle (Fuel Cells Materials) were used to prepare BSCF paste. The BSCF electrodes were screen-printed on the SDC surface, and sintered at 1,000 °C for 2 h with a heating and cooling rate of 1 °C min^{-1}. The average thickness of the printed electrodes was 12 μm.
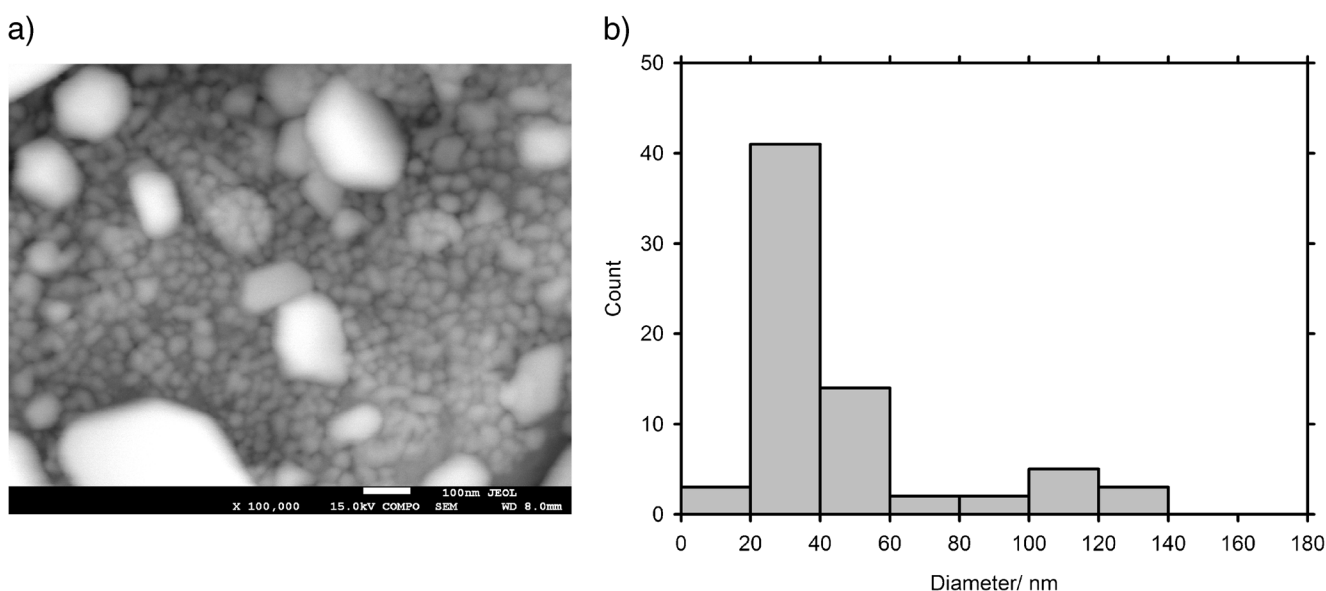
Fig. 7 **a** SEM image of Ag-BSCF composite powders (scan bar=100 nm); **b** histogram of the size distribution of the silver particles on the BSCF surface

Fig. 8 The diffraction pattern of the obtained Ag-BSCF powder. The diffractograms are shifted upwards with increasing annealing time: not sintered, sintered cathode, and sintered cathode after 48 h of tests at 600 °C, respectively. Reflexes are marked: *asterisk* regular BSCF phase, *diamond* $(Ba,Sr)CO_3$, *heart* silver, *triangle* hexagonal BSCF phase
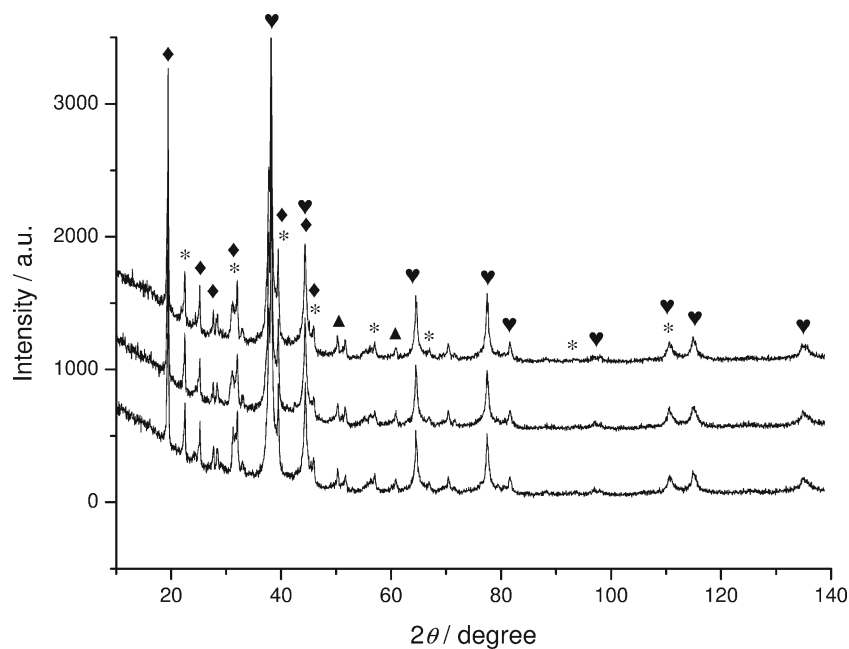
The Ag-BSCF powder obtained as described in Synthesis of silver nanoparticles and preparation of Ag-BSCF composite powders and an organic vehicle (Fuel Cells Materials) were used to prepare the Ag-BSCF paste, using method (1). The BSCF electrodes were screen-printed on the SDC surface, and sintered at 1,000 °C for 2 h with a heating and cooling rate of 1 °C min^{-1}.

The Ag-BSCF electrode was prepared through modification of the BSCF cathode with silver, using method (2). The method of nitrate decomposition was applied for this purpose: 0.05 mol dm^{-3} of $AgNO_3$ solution was added by drops, using a suction pipette accurate to 0.01 ml, and poured into the porous BSCF cathode layer placed on a heated hot plate to evaporate water, followed by firing at 800 °C for 6 h.

The BSCF powder was pressed into the form of a pellet, which was then sintered at 1,100 °C for 5 h with a heating and cooling rate of 1 °C min^{-1}, and finally cut by a diamond saw. The obtained ingots, 2 mm×1 mm, were crushed into pieces 4-mm long. The cross-sectional surface was rough, with many crystals oriented at angles between 30 and 60° to the surface, with protruding corners. This surface was used as a quasi-point electrode (Fig. 5d).

Methods

*XRD, SEM, X-ray fluorescence*

The phase composition of all powders and sintered samples was identified by XRD analysis based on the ICDD database. XRD measurements were performed using the PANalytical X'Pert Pro system with monochromatic CuK$_a$ radiation. The microstructure observations were carried out by means of a JEOL JSM-7500F field emission apparatus with an INCA PentaFETx3 EDS system. Chemical composition of investigated solids was determined with an Orbis Micro-EDXRF analyzer with a Rh anode as an X-ray source (operating at 30 kV and 400 mA) and Si(Li) detector, using Orbis Vision software, a system enabling multielement detection for elements from sodium to uranium.

EIS, CV, and long-time polarization measurements

The test fixture (see cross-section Fig. 5a) consists of a gastight outer alumina tube 300-mm long and an inner alumina tube with six channels (see cross-section Fig. 5b). A spring
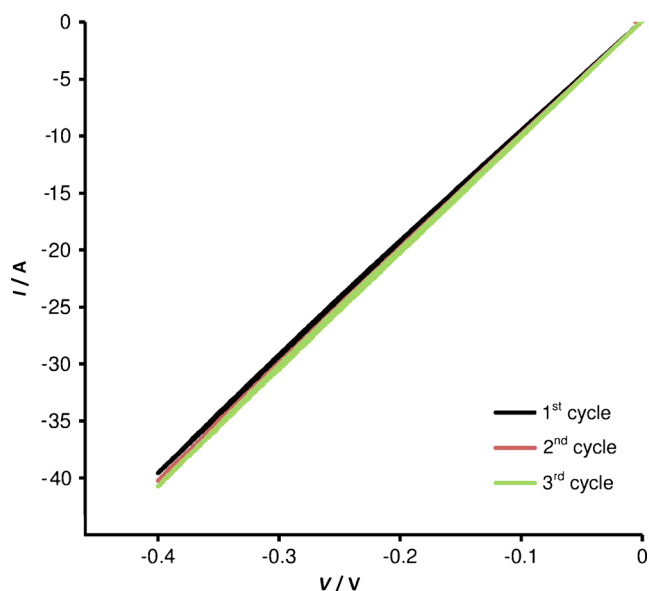
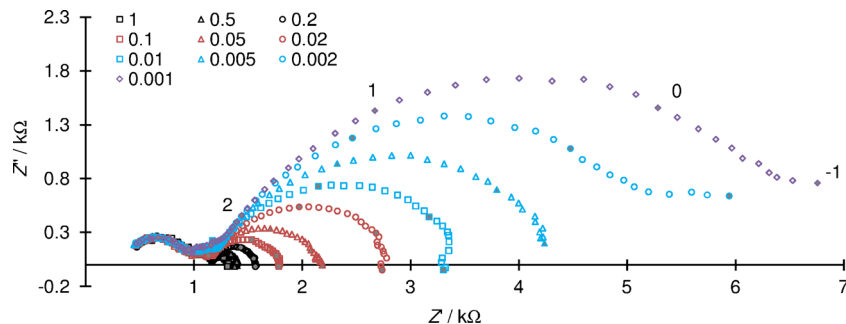**Fig. 9** CV of quasi-point BSCF electrode at 600 °C in air
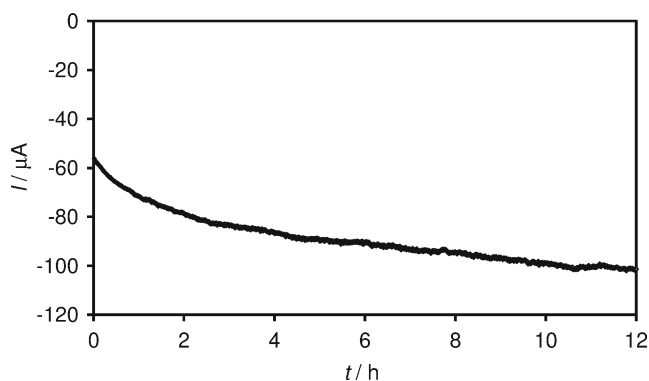
Fig. 10 Current recorded during the long-time polarization experiment: quasi-point BSCF electrode, −0.5 V, 600 °C

located in the beginning of the central canal presses on an alumina rod, which presses in turn on the cell elements, joining them together. Platinum wires connecting the cell to the potentiostat are located in three of the five smaller channels. The fourth is used for the thermocouple, the fifth as the gas inlet. The narrow channel in the front of the spring is used as a gas outlet. The details of the cell with three electrodes are sketched in Fig. 5c, d. Platinum wires terminating in platinum foil are used to connect with the potentiostat. Two steel (SUS 430, Ningbo Institute of Materials Technology & Engineering) plates are used as current collectors. The electrode, made of porous BSCF with a diameter of 5 mm, was screen-printed on one side, while the LSCF porous electrode, printed on the whole surface of the back side of the electrolyte, served as the counter electrode. The details of the cell are sketched in Fig. 5c, d.

EIS measurements were performed using a Gamry Series G 300 potentiostat/galvanostat/ZRA in a three-electrode setup (Fig. 5c, d) at rest potential in the frequency range from 0.01 to 300,000 Hz, with the amplitude of the sinusoidal voltage signal at 5 mV with a density of ten points per decade.

Every series of measurements began with 8 h of system equilibration at a temperature of 700 °C in oxygen. The dependency of impedance on the potential and concentration of oxygen was measured in mixtures of 99.95 % oxygen and 99.999 % argon (Linde Gaz Polska) in predetermined proportions. The flow rate of gas through the cell was 150 cm^3/min. The equilibration time after each change in oxygen concentration was 15 min.

For analysis of the impedance data, the Minuit [65] program, based on a complex nonlinear regression least-square procedure, was used to fit the equation describing the assumed equivalent electrical circuit (EEC) to the measured data. The quality of the fit was characterized by the standard deviation s, calculated from the formula as follows:

$$s = \sqrt{\frac{\sum_{1}^{n}\left(\frac{\text{Modulus}\left(Z_{i,measured}-Z_{i,fitted}\right)}{\text{Modulus}\left(Z_{i,measured}\right)}\right)^2}{n-1}} \qquad (3)$$

where Z_i is the impedance at the frequency number i.

The CV was performed in the three-electrode setup presented in Fig. 5, with a scan rate of 5 mV s^{-1}. The long-time polarization experiment was performed using the Gamry software written for chronoamperometry measurements, with the same electrode polarized at −0.5 V for 18 h.

Fuel cell testing

The following solid oxide fuel cells were tested:

H$_2$ |Ni–GDC|SDC|BSCF-GDC|BSCF
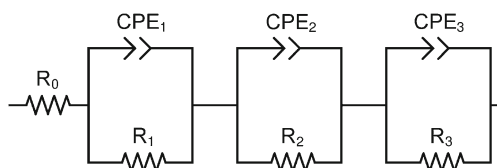H$_2$ |Ni–GDC|SDC|BSCF-GDC|Ag-BSCF

where Ni–GDC was anode material, SDC was an electrolyte disk 1.5-mm thick, and BSCF-GDC was composite cathode material obtained from BSCF+5 % mol GDC, BSCF, and Ag-BSCF investigated cathode materials. The electrochemical setup and details of the procedure for electrochemical measurements were described in previous papers [16, 33, 47]. Humidified hydrogen (3 wt.% H$_2$O) was used as a fuel and air as an oxidant. The flow rate of hydrogen was about 30 ml min^{-1}.

Results and discussion

Ag-BSCF composite nanopowder

Figure 6 shows typical SEM images of the Ag-BSCF composite, where the silver nanoparticles were obtained via the

Fig. 11 EIS spectra at 600 °C at various oxygen concentrations (in the legend in dimensionless P_{O2}/P) at quasi-point BSCF electrode; the numbers near filled symbols denote the logarithm of the frequency
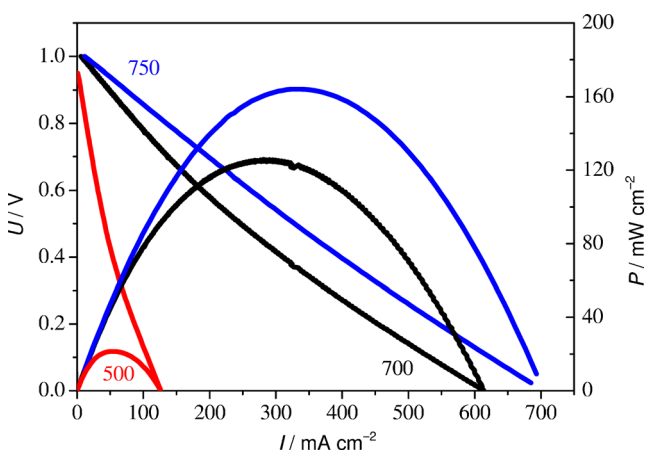
Fig. 12 Equivalent electrical circuit used to fit the data

reduction of silver nitrate by ethanol in the presence of PVP. As can be observed, the silver nanoparticles were uniformly distributed on the BSCF skeleton (Fig. 6a) and were incorporated into the porous BSCF matrix (Fig. 6a, b).
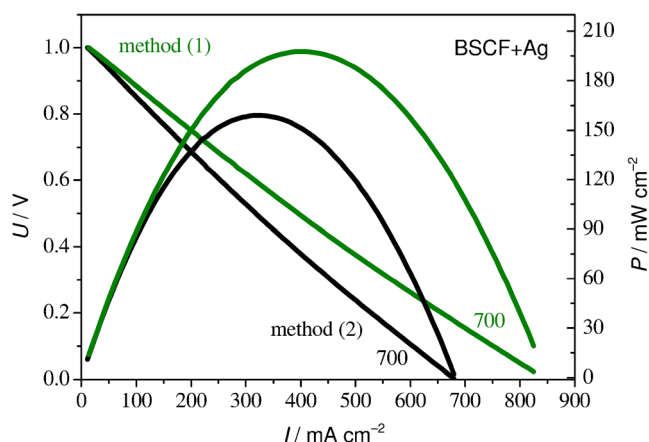
Furthermore, as can be seen (Fig. 6), the silver nanoparticles deposited on the BSCF appeared to be bimodal. To confirm this observation, a histogram of silver nanoparticles attached only to the BSCF surface was produced (Fig. 7). The micrograph and histogram presented below unambiguously indicated that the BSCF was covered by Ag particles with an average assumed size of 31 nm; however, there were a few larger particles with diameters greater than 100 nm. This result correlated quite well with the particle diameters measured in bulk by DLS (36 and 92 nm) and on the mica surface by SEM (31 nm) and presented in "Synthesis of silver nanoparticles and preparation of Ag-BSCF composite powders".

The comparison between unsintered Ag-BSCF powder, the sintered Ag-BSCF cathode, and the Ag-BSCF cathode after 48 h of testing are shown in Fig. 7. There are only very small differences between these diffractograms. Present are silver, regular BSCF phase, a small amount of hexagonal BSCF phase, and $(Ba,Sr)CO_3$ phase (Fig. 8).

The planned silver content was 34 %. When checked by the X-ray fluorescence (XRF) method in the obtained composite powder, this value was 43.5 %; after electrochemical tests in the composite cathode material, it was 42.4 %. In the cathodes obtained by method (2) after electrochemical tests, the measured by XRF method silver content was 41.9 %, whereas 40.0 % was planned.


Fig. 14 Family of curves (U–I and P–I) recorded for an IT-SOFC with a composite Ag-BSCF cathodes

Electrochemical measurements

Quasi-point BSCF electrode

The CV presented in Fig. 9 reveals no reduction or adsorption peaks in the measured range, but in the second and the third cycles, higher and higher currents were recorded; whereas in CV measurements in ranges −0.2 to 0.0 V and −0.3 to 0.0 V, the rise in current was not observed. The flowing current may be a reason for the decrease in electrode resistance. This was checked in a long-time polarization experiment (Fig. 10). The current increased more than twice within 18 h of polarization at −0.5 V. The rise in current can be explained by sintering BSCF cathode to the SDC electrolyte. The polarization speeds up this process. It is in accordance with results presented by Kim et al. [8]. These authors performed electrochemical cell tests of SOFCs containing an unsintered BSCF cathode at 700 °C and reported a good performance.

Fig. 13 Family of curves (U–I and P–I) recorded for an IT-SOFC with a monophase BSCF cathode
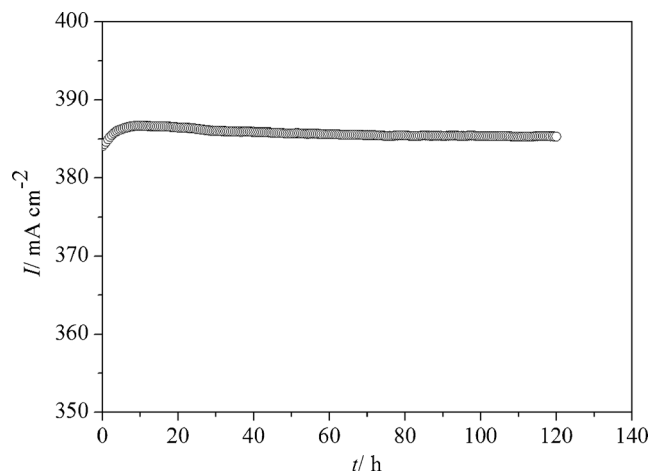
Fig. 15 Current recorded using IT-SOFC with Ag-BSCF cathode (method (1)) during 120 h

EIS spectra

EIS is a powerful technique used to study electrode reaction mechanisms, enabling the separation of reaction steps according to timescale [66]. Each slow reaction step can be reflected in a Nyquist plot of impedance spectra as a semicircle. The identification of steps can be improved performing measurements in different conditions (oxygen concentration, temperature, and potential). The impedance spectra of investigated electrodes are presented in Fig. 11 in a Nyquist representation. The EEC most frequently used (in cases where a more sophisticated EEC is not previously recommended for the electrode in question) consists of a resistor and several resistor-and-capacitor (R, C) pairs connected in series. Each pair reflects at least one slow step of the electrode reaction. Instead of a capacitor, a constant phase element (CPE) can be used. The impedance of the CPE may be expressed by the following formula [67]:

$$Z_{\mathrm{CPE}} = \frac{1}{\omega_0 C_0}\left(\frac{\omega_0}{j\omega}\right)^{\alpha} \quad (3)$$

where ω is the angular frequency, ω_0 is the angular frequency of reference, C_0 is the capacitance at the angular frequency of reference, and α is a coefficient close to 1 for an ideal capacitor, usually assuming a value between 0.7 and 1.0 in the case of nonideal capacitance. In our case, the frequency of reference was assumed to be 1,000 Hz. The same CPE element may represent the diffusional (Warburg) impedance, but coefficient α in this case is 0.5.

The spectra of the quasi-point BSCF electrode presented in Fig. 11 consist of two well-developed semicircles and a short straight segment (middle frequency semicircle) between them. The diameter of the high-frequency semicircle does not depend on oxygen concentration, whereas that of the low-frequency one does. For BSCF, the quasi-point electrode EEC presented in Fig. 12 was used. This kind of EEC can be fitted to the spectra containing three discernible semicircles. The resistance depends on oxygen concentration according to the following formula:

$$\log(R) = a - m\log(P_{\mathrm{O2}}) \quad (4)$$

where a and m are coefficients.

According to [59], m gives information about the reaction order. For R_0, R_1, R_2, and R_3, the coefficient m is equal to -0.0002, -0.017, -0.0059, and 0.53 respectively. The value $m=0.53$ may point to a charge transfer reaction with molecular oxygen involved, or to the diffusional impedance of molecular oxygen. The α parameter of a parallel CPE can help us to discern between both cases. It varies from 0.94 to 0.66 for oxygen partial pressures from 1 to 0.001, respectively, indicating the charge transfer reaction resistance.

Electrochemical tests of hydrogen-oxygen IT-SOFC

Figures 13 and 14 present the family of curves (U–I and P–I) recorded for an IT-SOFC with an SDC electrolyte and monophase BSCF or a composite Ag-BSCF cathode, respectively, within a temperature range of 500–750 °C, obtained with composite cathode materials via different preparation routes. As can be seen, an increase in power P and current density I was observed for the IT-SOFC with SDC and the Ag-BSCF composite cathode compared to the same IT-SOFC with only monophase BSCF material. The highest values for power density within the investigated temperature range were found for the Ag-BSCF composite cathode obtained via the new wet route. This could be related to the uniform distribution of silver particles on the BSCF cathode material at the stage of synthesis.

In a subsequent experiment, a 120-h stability test was completed with a voltage load of $\Delta E=0.5$ V, presented in Fig. 15. A stable current was observed during IT-SOFC operation under the applied current load. The preliminary results showed that Ag-BSCF obtained by method (1) seems to be a promising material for IT-SOFC application.

Conclusions

A new wet route for Ag-BSCF composite cathode powder is proposed. Silver nanoparticles obtained via one-step synthesis under absolute ethanol were used for the first time to prepare Ag-BSCF composite. The applied nanoparticles homogeneously dispersed on the surface and inside porous BSCF, which increased electrode performance. An IT-SOFC cell with composite cathode Ag-BSCF material exhibited better performance compared to a BSCF cathode by 48 %.

References

1. Juhl M, Primdahl S, Manon C, Mogensen M (1996) J Power Sources 61:173–181
2. Tsipis EV, Kharton VV (2011) J Solid State Electrochem 15:1007–1040
3. Shao ZP, Haile SM (2004) Nature 431:170–173
4. Zhou W, Ran R, Shao Z (2009) J Power Sources 192:231–246

5. Baumann FS, Maier J, Fleig J (2008) Solid State Ionics 21–26:1198–1204
6. Baumann FS, Fleig J, Habermeier H-U, Maier J (2006) Solid State Ionics 177:3187–3191
7. Liu QL, Khor KA, Chan SH (2006) J Power Sources 161:123–128
8. Kim Y-M, Kim-Lohsoontorn P, Baek S-W, Bae J (2011) Int J Hydrogen Energy 36:3138–3146
9. Schmale K, Barthel J, Bernemann M, Grünebaum M, Koops S, Schmidt M, Mayer J, Wiemhöfer H-D (2013) J Solid State Electrochem 17:2897–2907
10. Zhao H, Shen W, Zhu Z, Li X, Wang Z (2008) J Power Sources 182:503–509
11. Talaei ZS, Salamati H, Pakzad A (2010) Int J Hydrogen Energy 35:9401–9404
12. Yan A, Liu B, Dong Y, Tian Z, Wang D, Cheng M (2008) Appl Catal B Environ 80:24–31
13. Wang Y, Wang S, Wang Z, Wen T, Wen Z (2007) J Alloys Compd 428:286–289
14. Zhou W, Shao Z, Ran R, Zeng P, Gu H, Jin W, Xu N (2007) J Power Sources 168:330–337
15. Baker R, Guindet J, Kleitz M (1997) J Electrochem Soc 144:2427–2432
16. Mosiałek M, Dudek M, Wojewoda-Budka J (2013) Arch Metall Mater 58:275–281
17. Camaratta M, Wachsman E (2007) Solid State Ionics 178:1411–1418
18. Mosiałek M, Nowak P, Dudek M, Mordarski G (2014) Electrochim Acta 120:248–257
19. Guo Y, Liu Y, Cai R, Chen D, Ran R, Shao Z (2012) Int J Hydrogen Energy 37:14492–14500
20. Gao Z, Mao Z, Huang J, Gao R, Wang C, Liu Z (2008) Mater Chem Phys 2–3:290–295
21. Gao Z, Zhang P, Gao R, Huang J, Mao Z (2008) J Wuhan Univ Technol 23:350–353
22. Huang S, Zhou G, Xie Y (2008) J Alloys Compd 464:322–326
23. Akhtar N, Decent SP, Kendall K (2009) Int J Hydrogen Energy 34:7807–7810
24. Huang S, Zong Z, Peng C (2007) J Power Sources 173:415–419
25. Camaratta M, Wachsman E (2007) Solid State Ionics 178:1242–1247
26. Xia CR, Zhang Y, Liu ML (2003) Appl Phys Lett 82:901–903
27. Sasaki K, Hosoda K, Lan TN, Yasumoto K, Wang S, Dokiya M (2004) Solid State Ionics 174:97–102
28. Liu Y, Mori M, Funahashi Y, Fujishiro Y, Hirano A (2007) Electrochem Commun 9:1918–1923
29. Simner SP, Anderson MD, Coleman JE, Stevenson JW (2006) J Power Sources 161:115–122
30. Liu Y, Hashimoto S, Yasumoto K, Takei K, Mori M, Funahashi Y, Fijishiro Y, Hirano A, Takeda Y (2009) Curr Appl Phys 9:S51–S53
31. Sakito Y, Hirano A, Imanishi N, Takeda Y, Yamamoto O, Liu Y (2008) J Power Sources 182:476–481
32. Sholklapper TZ, Radmilovic V, Jacobson CP, Visco SJ, De Jonghe LC (2008) J Power Sources 175:206–210
33. Dudek M, Mosiałek M, Mordarski G, Socha RP, Rapacz-Kmita A (2011) Arch Metall Mater 56:1249–1255
34. Li Q, Sun L-P, Huo L-H, Zhao H, Grenier J-C (2011) J Power Sources 196:1712–1716
35. Su R, Lü Z, Jiang SP, Shen Y, Su W, Chen K (2013) Int J Hydrogen Energy 38:2413–2420
36. Zhou W, Ran R, Shao ZP, Cai R, Jin WQ, Xu NP, Ahn J (2008) Electrochim Acta 53:4370–4380
37. Su R, Lü Z, Chen K, Ai N, Li S, Wei B, Su W (2008) Electrochem Commun 10:844–847
38. Zhou W, Ran R, Cai R, Shao Z, Jin W, Xu N (2009) J Power Sources 186:244–251
39. Wang Z, Xu C, Lou Z, Qiao J, Ren B, Sun K (2013) Int J Hydrogen Energy 38:1074–1081
40. Chen Y, Wang F, Chen D, Dong F, Park HJ, Kwak C, Shao Z (2012) J Power Sources 210:146–153
41. Guo Y, Zhou Y, Chen D, Shi H, Ran R, Shao Z (2011) J Power Sources 196:5511–5519
42. Simner SP, Anderson MD, Templeton JW, Stevenson JW (2007) J Power Sources 168:236–239
43. Sarikaya A, Petrovsky V, Dogan F (2012) J Mater Res 27:2024–2029
44. Zhang Y, Liu J, Huang X, Lu Z, Su W (2008) Solid State Ionics 179:250–255
45. Haanappel VAC, Rutenbeck D, Mai A, Uhlenbruck S, Sebold D, Wesemeyer H, Röwekamp B, Tropartz C, Tietz F (2004) J Power Sources 130:119–128
46. Uhlenbruck S, Tietz F, Haanappel V, Sebold D, Buchkremer H-P, Stöver D (2004) J Solid State Electrochem 8:923–927
47. Mosiałek M, Tatko M, Dudek M, Bielańska E, Mordarski G (2013) Arch Metall Mater 58:1341–1345
48. Komarneni S, Li D, Newalkar B, Katsuki H, Bhalla AS (2002) Langmuir 18:5959–5962
49. Balaji DS, Basavaraja S, Deshpande R, Mahesh DB, Prabhakar BK, Venkataraman A (2009) Colloids Surf B 68:88–92
50. Michna A, Adamczyk Z, Oćwieja M, Bielańska E (2011) Colloids Surf A 377:261–268
51. Chen D, Qiao X, Qui X, Chen J (2009) J Mater Sci 44:1076–1081
52. Jiménez R, Kloidt T, Kleitz M (1997) J Electrochem Soc 144:582–585
53. Tomczyk P, Żurek S, Mosiałek M (2009) J Electroceram 23:25–36
54. Wang L, Merkle R, Maier J (2010) J Electrochem Soc 157:B1802–B1808
55. Choi J, Park I, Lee H, Shin D (2012) Solid State Ionics 216:54–57
56. Hieu NT, Park J, Tae B (2012) Mater Sci Eng B 177:205–209
57. Lee SO, Lee D, Jung I, Kim D, Hyun S-H, Kim J, Moon J (2013) Int J Hydrogen Energy 38:9320–9329
58. Patra H, Rout SK, Pratihar SK, Bhattacharya S (2011) Int J Hydrogen Energy 36:11904–11913
59. Liu B, Zhang Y, Zhang L (2009) Int J Hydrogen Energy 34:1008–1014
60. Sakai N, Yamaji K, Horita T, Xiong YP, Kishimoto H, Brito ME, Yokokawa H (2004) Solid State Ionics 174:103–109
61. Ivers-Tiffée E, Weber A, Schmid K, Krebs V (2004) Solid State Ionics 174:223–232
62. Hashibon A, Raz S, Riess I (2002) Solid State Ionics 149:167–176
63. Dudek M (2008) J Eur Ceram Soc 28:965–971
64. Kim J-S (2007) J Ind Eng Chem 13:566–570
65. James F, Roos M (1975) Comput Phys Commun 10:343–367
66. Adler SB (2004) Chem Rev 104:4791–4843
67. Simka W, Mosiałek M, Nawrat G, Nowak P, Żak J, Szade J, Winiarski A, Maciej A, Szyk-Warszyńska L (2012) Surf Coat Technol 213:239–246